Facile Dissolution−Crystallization Strategy to Achieve Rapid and Uniform Distribution of Sulfur on Porous Carbon for Lithium−Sulfur Batteries

Hui Zhang, Geng Gao, Yin Li, Keyu Zhang, Yaochun Yao,* and Shaoze Zhang*

Read Online

ACCESS | Metrics & More | Article Recommendations

ABSTRACT: In this work, we proposed a facile dissolution−crystallization strategy based on density functional theory calculations to achieve rapid as well as uniform distribution of sulfur on porous carbon. Sulfur-containing solution can completely penetrate porous material and in preference remove into the pores under the influence of capillary force, and sulfur tends to crystallize on the defective even non-defective carbon matrix rather than agglomerate. The S/ PC composites prepared by this method can still achieve uniform distribution of sulfur when the sulfur content is as high as 85%. All operations can be completed within a few minutes without any heating. Compared with common melt-diffusion and vapor-phase infusion, this approach has lower energy consumption and is simple, safe, continuous, and rapid.
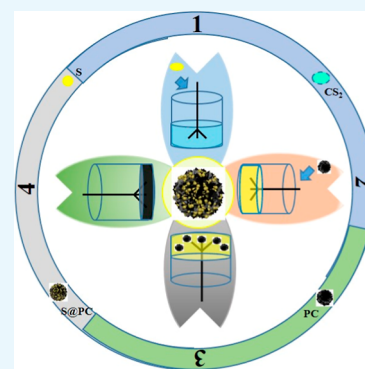
1. INTRODUCTION

Modern living standards create higher demands for power, energy density, and cycling durability of the energy storage system.[1,2] Lithium−sulfur batteries are extensively studied as a propitious energy storage system because of their high theoretical specific capacity of 1675 mAh g^{-1} and energy density of 2600 Wh kg^{-1},[3−6] environmental friendliness, abundant resources, and low price.[7] However, the poor conductivity of sulfur and its reduction products Li_2S/Li_2S_2 is responsible for the low active material utilization and poor rate capability. At the same time, the volume expansion of sulfur and the shuttle effect caused by the dissolution of polysulfide in the electrolyte lead to attenuation of battery capacity.[8] For that reason, sulfur is normally encapsulated in a porous conductor matrix, such as graphene,[9] carbon nano-tubes,[10] or porous carbon,[11] that can facilitate electron transport, buffer the volume expansion, and trap the polysulfide.

Usually, melt-diffusion and vapor-phase infusion methods are high-frequency approaches to confined sulfur in a carbon material.[12] At high temperatures, molten sulfur or gaseous sulfur infiltrates into a hollow space under the action of the capillary force and then solidifies and aggregates during the cooling process. Both of them require a long heating time for sulfur to melt, sublimate, and migrate. The lengthened heating leads to reduced productivity and increased energy consumption.[13] In addition, molten sulfur only exhibits partial moistening with a rough contact angle of 50° on the carbon surface.[14] The high diffusion resistance of molten sulfur always

creates uncontrollable sulfur coating on carbon materials. Sometimes, the functionalized carbon surface is used to enhance chemical binding of LiPSs. Unfortunately, it also hinders the inward diffusion of sulfur.[12] Therefore, it is still a huge challenge for sulfur to infiltrate the entire surface of the carbon material and deposit uniformly.

In this work, density functional theory (DFT) calculations provided details about the interaction of S_8 with models of porous carbon. Herein, we propose a facile dissolution−crystallization strategy under the guidance of DFT to achieve rapid as well as uniform distribution of sulfur on porous carbon. Since sulfur can be effortlessly dissolved in carbon disulfide at ambient temperature and pressure, the amount of the solution can be arranged to ensure that they completely penetrate porous material and in preference remove into the pores under the influence of capillary force. With the volatilization of solvent, sulfur tends to precipitate on the defective even on the non-defective carbon matrix rather than agglomerating. As long as carbon has a considerable specific surface area, sulfur can be dispersed uniformly until it reaches the size of a nanometer. All operations can be completed
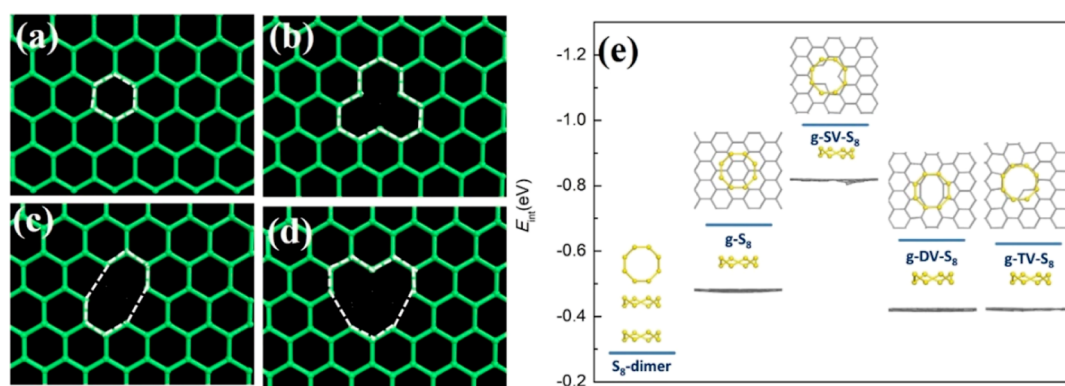
Figure 1. Models of porous carbon: (a) ideal graphene; graphene with (b) SV; (c) DV; (d) TV; (e) the interaction energies (E_{int}) for different systems in this study: S_8 dimer, S_8 molecule adsorbs on graphene (g-S_8), S_8 molecule adsorbs on graphene with SV (g-SV-S_8), S_8 molecule adsorbs on graphene with DV (g-DV-S_8), and S_8 molecule adsorbs on graphene with TV (g-TV-S_8). For each structure inset, the top picture is the top view and the bottom is the side view.

within a few minutes without any heating. Compared with melt-diffusion and vapor-phase infusion, this approach has lower energy consumption and is simple, safe, continuous, and rapid. Therefore, it is suitable for the composition of sulfur with porous carbon, even for other porous material matrix and especially for the material modified by heating during the sulfur loading process.

2. COMPUTATIONAL METHODOLOGY

All the periodical DFT calculations were employed by the Vienna Ab initio Simulation Package (VASP).[15−18] The Perdew−Burke−Ernzerhof exchange−correlation function,[19] with projector-augmented wave scheme,[20] was applied to report the ion-electron exchange−correlation. The DFT-D3,[21] including Becke−Johnson damping,[22] was utilized to correct the long-range dispersion. The energy cutoff for the plane-wave expansion was set up to 450 eV. The Brillouin zone integration was generated according to the Monkhorst−Pack method[23] using a Gamma centered $2 \times 2 \times 1$ k-point mesh. All structures were relaxed until the energy changed to less than 1×10^{-5} eV, with the forces on each atom being below 0.01 eV/Å.

On a short length scale, porous carbon can be considered as a combination of an integral graphene layer and a graphene layer with defects. To mimic the porous carbon materials, four types of graphene-relevant surfaces are constructed. These models simplify the non-uniformity graphite carbon layer by locally considering ideal graphene and ideal graphene containing single vacancy (SV), doublet vacancies (DV) and triplet vacancies (TV).[24] Sulfur is regarded as a stabilized form of S_8. A vacuum slab of 15 Å is added alongside the c axis to diminish the interactions between adjacent cells arising from the periodic effect. In this work, the interaction energy (E_{int}) is calculated and defined as

$$E_{int} = E_{system} - \sum_i E_i \qquad (1)$$

E_{system} is the total electronic energy for the whole optimized complex, and the E_i is the energy of the isolated fragment, including the S_8 molecule and four types of graphene-relevant surfaces.

Carbon with four different models, pristine graphene layer, SV, DV, and TV on the graphene layer, is shown in Figure 1a−d. As a result, two pentagons and one octagon defects take the shape in reconstructed DV and two 5-membered rings and one

10-membered ring are formed in reconstructed TV. After structure optimization, S_8 was absorbed on the four slabs. The interaction energies of these four configurations were −0.68, −0.99, −0.63, and −0.62 eV, respectively. The adsorptions between S_8 and porous carbon are stronger than that between the S_8 dimer, which is the E_{int} value calculated to be −0.29 eV, indicating that the S_8 molecule tends to be adsorbed onto the carbon porous surface rather than the agglomerate themselves.

Taking the mechanism of crystal nucleation and growth into consideration, a carbon matrix is reasonable to be a heterogeneous nucleus for sulfur crystallization. As long as carbon has a considerable specific surface area, sulfur can be dispersed uniformly on the carbon surface during the crystallization process until it reaches the size of a nanometer. It is worth noting that the defects in graphene only play a role in the first dissociation event, and the interface interaction after the model adsorbs sulfur needs to be calculated separately.

3. EXPERIMENTAL SECTION

3.1. Preparation of Mesoporous Carbon. Natural tubular corn silk was selected to be the carbon source to fabricate porous carbon. Dried corn silk was calcined and activated by K_2CO_3 at 800 °C in a vacuum tube furnace. The remnant was washed several times by deionized water to meet the pH value 7, then dried, and ground.

3.2. Synthesis of S/PC Composites. Carbon disulfide (2 mL) was used to dissolve 0.233 g of sublimated sulfur, then 0.1 g of as-prepared porous carbon was added into the solution, and continuously stirred until the carbon disulfide completely volatilized naturally. The composite was washed by absolute ethanol multiple times until the residual of carbon disulfide was removed. In the end, the composite was kept in a vacuum oven at 60 °C for 6 h. This sample was denoted as 70S/PC. Using the same method, samples containing 75, 80, and 85% sulfur were prepared respectively and be noted as 75S/PC, 80S/PC, and 85S/PC. The schematic illustration of the preparation process is shown in Figure 2.

3.3. Materials Characterization. The nitrogen physical adsorption/desorption isotherms were measured by a volumetric adsorption system (V-Sorb 2800TP) at 373 K. The phase structure was characterized by powder X-ray powder diffraction (XRD, D8 ADVANCE, Bruker) at a scan rate of 6° min⁻¹ from 5° to 90°. Raman spectra were recorded on a laser confocal micro-Raman spectroscope (LabRAM HR800) at a
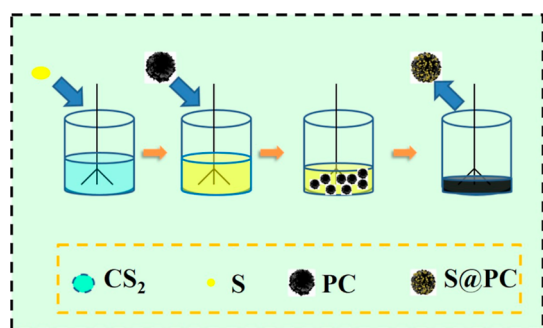
Figure 2. Schematic illustration of the preparation process of the S/PC composite.

632.8 nm excitation in the range of $100-3500$ cm^{-1}. Thermogravimetric analysis (TGA, Q500 TGA) was performed at a heating rate of 10 °C min^{-1} from room temperature to 800 °C in a nitrogen atmosphere. X-ray photoelectron spectroscopy (XPS, PHI-5000) was carried out with a monochromatic Al X-ray source (15 kV). The morphology and microstructure of materials were investigated by scanning electron microscopy (SEM, TESCAN, VEGA-3SBH) with energy-dispersive X-ray spectrometry (EDS) and high-resolution transmission electron microscopy (HRTEM, Tecnai G2 F20 S-TWIN).

3.4. Electrochemical Tests. The as-prepared S/PC composites were mixed with Super P and polyvinylidene fluoride at a ratio of 70:20:10 (wt %) to form a slurry by using N-methyl-2-pyrrolidone as the solvent and was pasted evenly onto an aluminum foil. The areal active material loading in all the composite cathodes is approximately 1.0 mg cm^{-2}. CR2025 coin cells were assembled in a glovebox with pre-prepared aluminum foil as the positive electrode, a metallic lithium film as the negative electrode, and 90 μL of 1.0 M LiTFSI and 0.1 M LiNO$_3$ in DME/DOL = 1:1 (vol %) as the electrolyte. The charging and discharging performances were recorded on a battery test system (Xinwei, BTS 9000) with the voltage ranging from 1.8 to 2.7 V. Cyclic voltammetry (CV) measurement was conducted at a scan rate of 0.1 mV s^{-1} on an electrochemical workstation (Princeton, PMC-2000). Electrochemical impedance spectroscopy (EIS) was performed on a cell before and after 100 cycles with the frequency ranging from 0.01 Hz to 100 kHz on the electrochemical workstation.

4. RESULTS AND DISCUSSION

SEM investigated the microscopic morphologies of the composites and portrayed the images in Figure 3. The composites have the same morphology, which indicates that the synthesis process does not change the structure of samples. The EDS image (Figure 3b−b3) reflects that sulfur has been uniformly loaded on the surface of the carbon pieces when the sulfur content added is as high as 85%. From high-magnification images, we can see that the porous carbon maintains an obvious pleated structure. This structure provides a high specific surface area to the carbon matrix, which can effectively increase the dispersion of crystal sulfur and reduce aggregation. Nanoscale sulfur particles are more likely to be stored in pores, dispersions, and pleated regions, which match with the results of DFT. Therefore, in order to ensure the nanometer size of sulfur crystals, the content of sulfur should
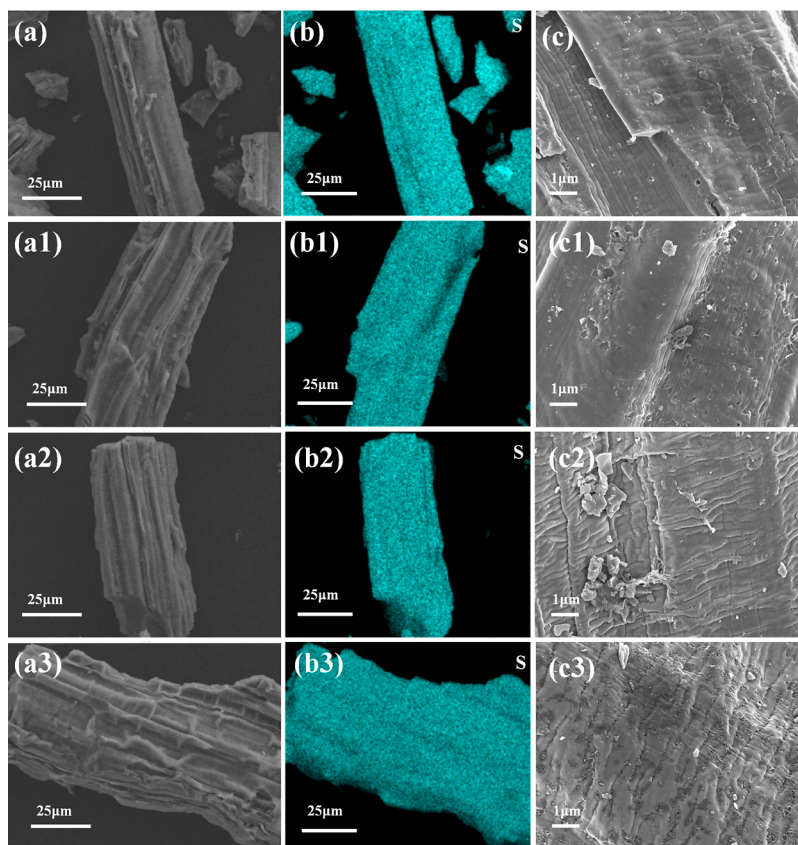

Figure 3. SEM images and mapping of composites (a−c) 70S/PC; (a1−c1) 75S/PC; (a2−c2) 80S/PC; and (a3−c3) 85S/PC.
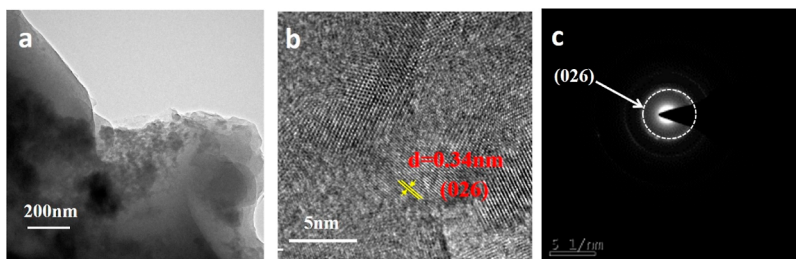
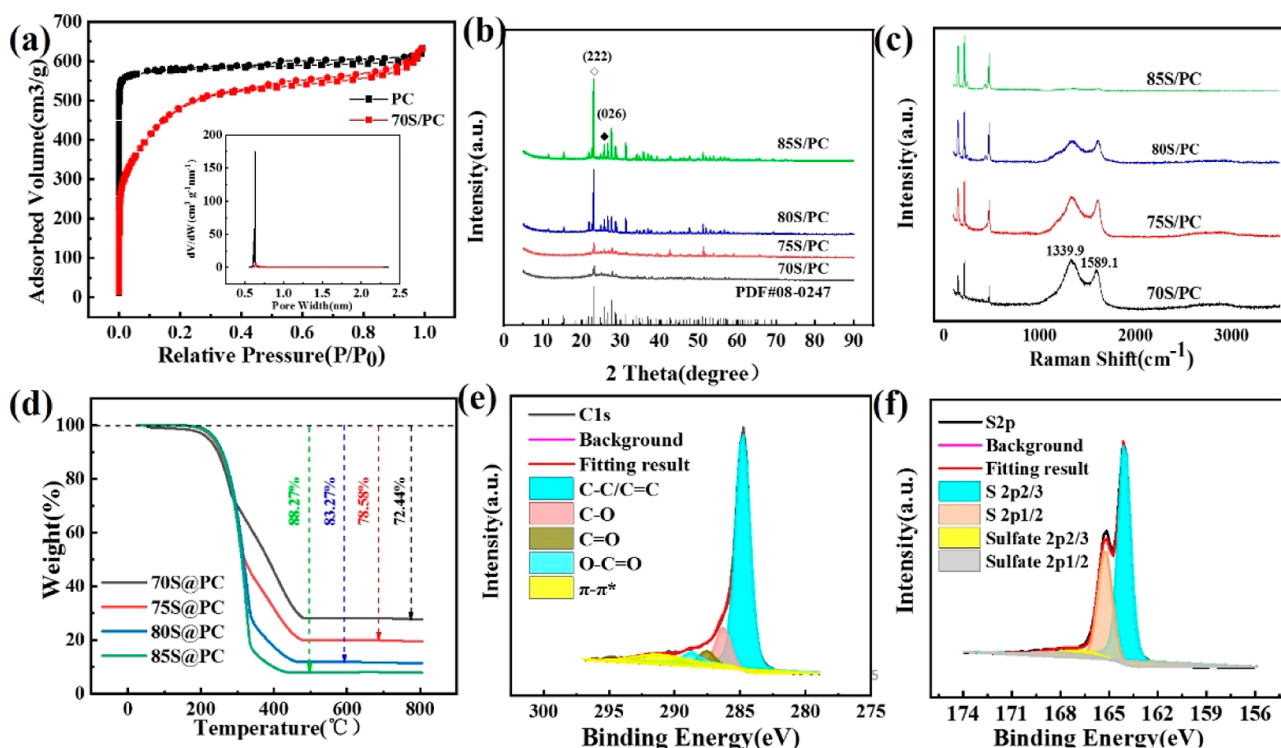**Figure 4.** (a,b) HRTEM images of the 70S/PC composite and (c) SEAD pattern of 70S/PC.

Figure 5. (a) Nitrogen adsorption/desorption isotherms; inner diagram: pore size distributions of PC and 70S/PC; (b) XRD patterns of composites; (c) TGA data of composites; (d) Raman spectrums for composites; and (e,f) XPS survey spectra and fitted photoelectron lines of the C 1s and S 2p of 70S/PC composite.

not be too high when the specific surface area and cumulative pore volume of the carbon particles are certain.

The deposition structure and contact between sulfur and carbon were further proven by the HRTEM diagram (Figure 4). The translucent carbon nanosheet shows that the porous carbon is very thin. Figure 4b shows a large number of micropores on the carbon surface and the sulfur appears in or nearby pores. It is tightly attached to the carbon skeleton through a thin layer. Clear lattice lines appear on the surface of carbon, indicating that the sulfur after crystallization has a complete crystal structure. According to the SEAD picture (Figure 4c), these lattice lines correspond to the (026) plane of sulfur crystal. It confirms that sulfur has a preferred crystal orientation on carbon.

The specific surface area and pore structure were characterized by nitrogen adsorption/desorption isotherms. Figure 5a shows a typical type I isotherm with a H4 reversible hysteresis loop, suggesting the existence of a large amount of micropores. When P/P_0 is lower than 0.02, the adsorption increases sharply, which is due to the micropore filling. The micropores are shaped like slits, indicated by the adsorption

curve becoming nearly horizontal.[25] A hysteresis loop at P/P_0 above 0.5 reflects the presence of mesopores. It is calculated that the specific surface area of PC can reach as high as 2390 m^2 g^{-1}, which is conducive to the dispersion of sulfur and reduces aggregation. The total micropore volume is 0.88 cm^3 g^{-1} by the T-plot method, corresponding to a theoretical loading of 68 wt % sulfur. The pore-size distribution curve (inner Figure 5a) reveals that micropores mainly distribute at around 0.62 nm, which is beneficial to the absorption of sulfur and LiPSs.[26] After synthesis with 70 wt % sulfur, the change of nitrogen adsorption/desorption isotherms indicates the reduction of the amount of micropores. The BET surface area of S/PC is reduced to 1752.69 m^2/g, while the total micropore volume dropped to 0.28 cm^3 g^{-1}. Calculated by the density of sulfur, 59% of the sulfur enters the carbon pores.

In Figure 5b, XRD analyzed and portrayed the crystal-like structure of the material. It could be seen that four composites have analogous diffraction peaks at the same positions except for the peak intensity. Generally, the peak of graphite at 26° is the characteristic peak of (002) planes. However, the peak of carbon used in composites in the XRD pattern is broadened
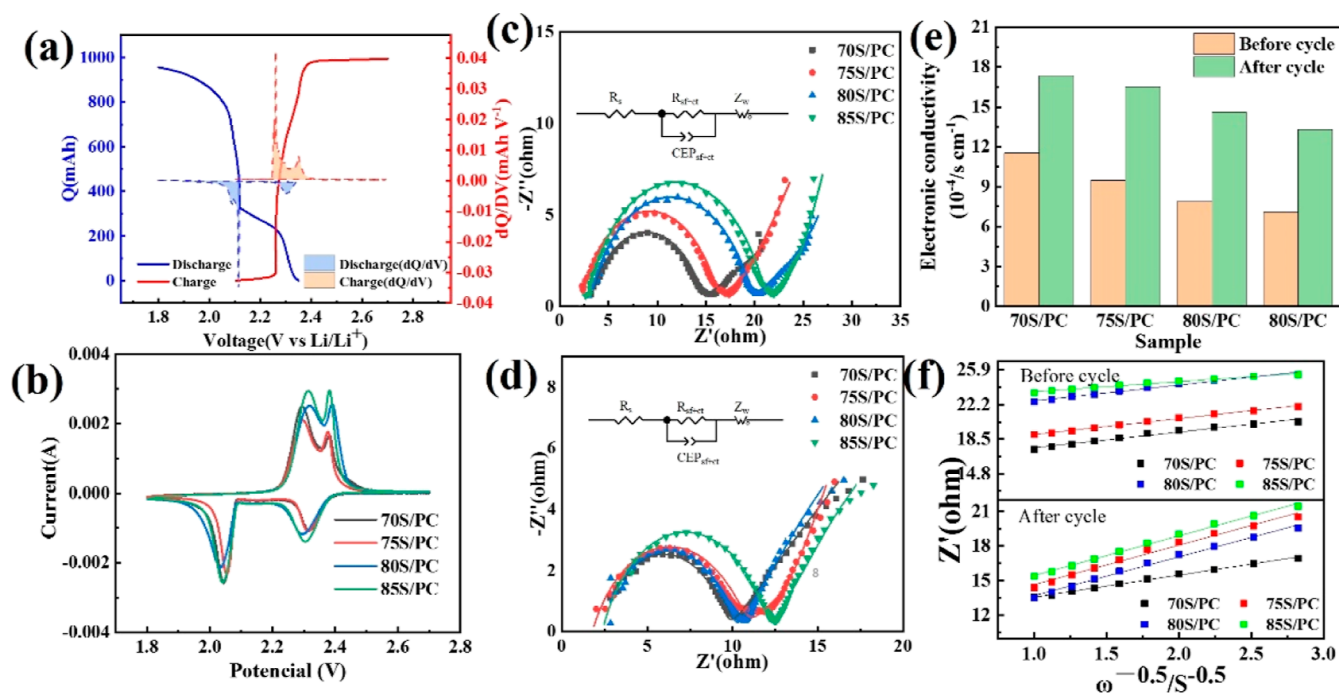
Figure 6. (a) dQ/dV curve of the 70S/PC composite; (b) cycle voltammetry curves of composites; Nyquist plots of composites (c) fresh cell; (d) after the 100th electrochemical cycle; (e) comparison of electronic conductivity before and after electrochemical cycle; and (f) relationship between Z_{re} and $\omega^{-0.5}$ at low frequencies before and after electrochemical cycle.

and shifted to a lower angle, indicating poor crystalline characteristics due to increased structural defects and expanded interlayer distances in the activation process.[25] The characteristic peaks centered around 23° correspond to the orthorhombic sulfur (222) planes indexed to element 08-0247 in JCPDS card. The absence of another diffraction peak reveals that no new phases were formed by the dissolution–crystallization method. With the increase of sulfur content, the intensity of the sulfur diffraction peaks increases and that of the carbon diffraction peaks decreases. The weak intensity of sulfur in the 70S/PC curve reflects that sulfur is preferentially deposited into the pores of carbon.[27] The higher the sulfur content, the more sulfur is deposited on the surface of the carbon, resulting in an increase in the peak intensity of sulfur. At the same time, due to the strong force between sulfur and carbon,[28] the intensity of the carbon peak gradually decreases.

To further verify that sulfur has been composited with a carbon skeleton, Raman tests were carried out, and the results are shown in Figure 5c. The two peaks around 1339.9 and 1589.1 cm^{-1} in the Raman spectra belong to the D, G characteristic peaks of carbon materials. With the increase of sulfur content, the intensity of sulfur diffraction peaks increases and the carbon diffraction peaks decreases. The weak characteristic peak of sulfur in 70s/PC reveals that sulfur is successfully confined in the carbon pores. Since the value of $I(D)/I(G)$ can reflect the degree of graphitization,[29] the value of curve from bottom to top is 1.33, 1.11, 1.04, and 0.91, respectively. The decrease of the value represents the reduction of the defects on carbon materials, which attribute to the more sulfur fill the carbon pores. The lesser magnitude of the carbon peak can be explained by the stronger interaction between sulfur and the oxygen group in the carbon materials.[30]

TGA is used to measure the amount of sulfur carried on the carbon skeleton. In the TGA graph (Figure 5d), the weight loss is close to the experimental arrangement, which shows that

the dissolution–crystallization method can accurately control the amount of sulfur loading. The slight deviation may be caused by the random distribution of mesopores on the carbon material. Since sulfur is deposited in the pores rather than simply mixed with carbon, the distribution of carbon pores determines the mount of loading sulfur. Obviously, the lower sulfur content of the composite has better thermal stability. Nanopores can protect sulfur well from sublimation, which proves that sulfur is preferentially crystallized in the pores. Therefore, we can infer that the pores also have a strong physical adsorption capacity for polysulfide, which is conducive to the cycle stability of the battery. As the sulfur content increases, the more sulfur is deposited on the surface of the carbon particles, the easier it is to evaporate.

XPS analysis further revealed the chemical structure and effects of introduction of sulfur, and the results are shown in Figure 5e,f. The characteristic peaks of C and S confirms the substance of composites, which is consistent with the XRD and Raman result. The O characteristic peak is determined by the oxygen groups in the biomass carbon material. The high-resolution C 1s spectral profiles (Figure 5e) can be deconvoluted into five peaks at 284.25, 285.75, 287.00, 288.20, and 290.73 eV,[31] which presents the C=C/C−C, C−O, C=O, O−C=O, and $\pi-\pi^*$, respectively. At the same time, the S 2p spectrum (Figure 5f) can be divided into four component peaks at 164.07, 165.25, 168.96, and 170.14 eV, which are attributed to the $2p_{3/2}$ and $2p_{1/2}$ of S element and the presence of S in R−SO$_3$−R$_0$.[30] Sulfate is considered to be caused from the reaction of S with the oxygen group in carbon materials; thus, sulfate reveals uniform distribution of sulfur and strong interaction between the carbon matrix and sulfur, which is supported by Raman testing.

We judge the reaction platform of the carbon−sulfur composite through the dQ/dV curve (Figure 6a). At about 2.30 and 2.11 V, the typical and characteristic reduction peaks
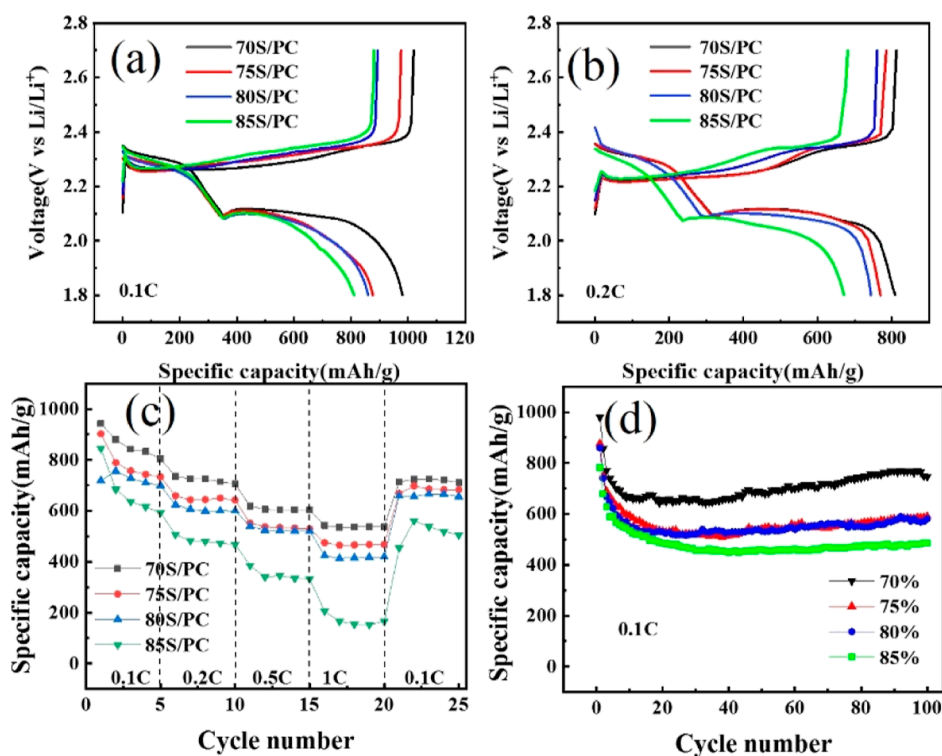
Figure 7. (a) First charge/discharge diagram of composites at 0.1 C; (b) first charge/discharge diagram of composites at 0.2 C; (c) rate performance of composites; and (d) cycling performance of composites at 0.1 C.

occur. This indicates the reduction of elemental sulfur to long-chain LiPSs and the continual reduction to short chain.[32] The process of Li_2S_2/Li_2S being oxidized to LiPSs and finally to sulfur corresponds to the peaks of oxidation that occur at about 2.28 and 2.35 V.[33] In the CV (Figure 6b) curves of composites, four samples have a similar shape. The potential at which the redox reaction occurs corresponds to the position of dQ/dV. The slight difference in reaction potential may be due to the poor conductivity of sulfur. The delay in electron transfer leads to the occurrence of cell polarization.

The reaction kinetics of the composites were verified by EIS, and the electronic conductivity and lithium ion diffusion coefficient (D_{Li^+}) were evaluated by fitting a Nyquist plot with an equivalent circuit.[34,35] The Nyquist curves of cells before and after discharge are depicted in Figure 6c,d. The equivalent circuit features the electrolyte solution resistance (R_s), the charge transfer resistance (R_{ct}) between the interface of the electrolyte and electrode, and the Warburg diffusion impedance of lithium ions in the positive electrode.[36] After calculating the relationship between Z_{re} and frequency, the R_{ct} and thickness of electrode materials, the values of electronic conductivity, and Li^+ diffusion coefficient are compared in Figure 6e,f. The fitting results show that with the increase of sulfur content, the R_{ct} values in fresh cells rise and the electronic conductivity of the composite drops. The electronic conductivity decreases caused by the poor conductivity of sulfur, which just confirms the increase of sulfur content in the composite. After 100 cycles, the R_{ct} of the composite material dropped together, causing the electronic conductivity to rise, but the trend did not change. The decrease of R_{ct} may be due to the fact that the discharge is advantageous to the redistribution of sulfur on the carbon matrix.[37] In contrast, the lithium ion diffusion coefficient of the composite decreases after the discharge cycle, which may be due to the increase of

viscosity and Li^+-transfer resistance that is caused by the dissolution of LiPSs in the electrolyte.[32]

The electrochemical performance of the composite material is measured by the discharge–charge measurement between 1.8 and 2.7 V. Figure 7a,b shows the charge/discharge curve of the first cycle at the C-rates of 0.1 and 0.2 C (1 C = 1675 mA h g^{-1}). For the electrode, there are two typical voltage plateaus at 2.3 and 2.1 V consistent with the position of the dQ/dV curve, which indicates a two-step transition from S to LiPSs and Li_2S_2/Li_2S. The length of the discharge platform reflects the capacity of the battery. From the figure, the capacity does not increase but decreases with the rise of sulfur content. The initial discharge capacity at 0.1 C is 980 mA h g^{-1} of 70S/PC, 876 mA h g^{-1} of 75S/PC, 859 mA h g^{-1} of 80S/PC, 782 mA h g^{-1} of 85S/PC, and 0.2 C is 809 mA h g^{-1}, 769 mA h g^{-1}, 743 mA h g^{-1}, and 671 mA h g^{-1}, respectively. More sulfur affects the transport of electrons and Li^+, making the electrochemical performance of the battery worse, which can also be confirmed on the rate performance (Figure 7c). The capacity retention of the composites after 100 cycles is 76, 67, 67, and 62%, respectively. The capacity retention rate decreases with the rise of the sulfur content. The reason is that the amount of LiPSs dissolved in the electrolyte increases, and the shuttle effect causes the capacity attenuation. All electrochemical performances show a regular correlation. The composites with high sulfur content exert relatively low sulfur utilization due to the small conductivity. Sulfur particles slow down the electron transfer and hinder the Li^+ transport. At the same time, the dissolution of LiPSs increases the shuttle effect and causes capacity degradation.

5. CONCLUSIONS

In summary, the S/PC composites were successfully synthesized through a simple dissolution-crystallized strategy

based on the theoretical calculation of sulfur crystallization on porous carbon. With the volatilization of solvent, sulfur was preferentially precipitated in the pores under the capillary force and homogeneously distributed on the carbon surface in nanometer-sized particles. All operations can be completed within a few minutes and without any heating. The electrochemical performance shows a regular trend. With the increase of the sulfur content, the specific capacity, rate performance, and capacity retention decrease, which is attributed to the poor conductivity. Sulfur particles slow down electron transfer and hinder the Li$^+$ transport. At the same time, the dissolution of LiPSs increases the shuttle effect and causes capacity degradation. This work not only offers a facile method to composite sulfur with porous carbon but also provides an idea for the economic and efficient production of lithium−sulfur batteries.

■ AUTHOR INFORMATION

Corresponding Authors

Yaochun Yao − *The National Engineering Laboratory for Vacuum Metallurgy, Kunming University of Science and Technology, Kunming 650093, China;* ⊙ orcid.org/0000-0001-6837-1789; Email: yaochun9796@163.com

Shaoze Zhang − *The National Engineering Laboratory for Vacuum Metallurgy, Kunming University of Science and Technology, Kunming 650093, China;* ⊙ orcid.org/0000-0001-9387-2462; Email: szzhang@kust.edu.cn

Authors

Hui Zhang − *The National Engineering Laboratory for Vacuum Metallurgy, Kunming University of Science and Technology, Kunming 650093, China; Material and Architecture College, Guizhou Normal University, Guiyang 550025, China*

Geng Gao − *The National Engineering Laboratory for Vacuum Metallurgy, Kunming University of Science and Technology, Kunming 650093, China*

Yin Li − *The National Engineering Laboratory for Vacuum Metallurgy, Kunming University of Science and Technology, Kunming 650093, China*

Keyu Zhang − *The National Engineering Laboratory for Vacuum Metallurgy, Kunming University of Science and Technology, Kunming 650093, China*

Complete contact information is available at:
https://pubs.acs.org/10.1021/acsomega.2c01217

Author Contributions

H.Z. performed the experiments and wrote the original draft. G.G. participated the electrochemical analysis. Y.L. and K.Z. participated the review and editing. Y.Y. coordinated and supervised the overall project. S.Z. checked the validity of DFT calculations. All authors discussed the results and participated in manuscript preparation.

Notes

The authors declare no competing financial interest.

■ ACKNOWLEDGMENTS

■ REFERENCES

(1) Wang, X.; Kim, H.-M.; Xiao, Y.; Sun, Y.-K. Nanostructured metal phosphide-based materials for electrochemical energy storage. *J. Mater. Chem. A* **2016**, *4*, 14915.

(2) Zhao, Y.; Li, X.; Yan, B.; Xiong, D.; Li, D.; Lawes, S.; Sun, X. Recent developments and understanding of novel mixed transition-metal oxides as anodes in lithium ion batteries. *Adv. Energy Mater.* **2016**, *6*, 1502175.

(3) Pang, Q.; Tang, J.; Huang, H.; Liang, X.; Hart, C.; Tam, K. C.; Nazar, L. F. A nitrogen and sulfur dual-doped carbon derived from polyrhodanine @ cellulose for Advanced Lithium-Sulfur Batteries. *Adv. Mater.* **2015**, *27*, 6021−6028.

(4) Weret, M. A.; Jeffrey Kuo, C.-F.; Zeleke, T. S.; Beyene, T. T.; Tsai, M.-C.; Huang, C.-J.; Berhe, G. B.; Su, W.-N.; Hwang, B.-J. Mechanistic understanding of the Sulfurized-Poly(acrylonitrile) cathode for lithium-sulfur batteries. *Energy Storage Mater.* **2020**, *26*, 483−493.

(5) Kuo, C. F. J.; Weret, M. A.; Hung, H. Y.; Tsai, M. C.; Huang, C. J.; Su, W. N.; Hwang, B. J. Sulfurized−poly(acrylonitrile) wrapped carbonesulfur composite cathode material for high performance rechargeable lithiumesulfur batteries. *J. Power Sources* **2019**, *412*, 670−676.

(6) Armand, M.; Tarascon, J.-M. Building better batteries. *Nature* **2008**, *451*, 652−657.

(7) Bruce, P. G.; Freunberger, S. A.; Hardwick, L. J.; Tarascon, J.-M. Li-O2 and Li-S batteries with high energy storage. *Nat. Mater.* **2012**, *11*, 19−29.

(8) Han, X.; Cai, J.; Wang, X.; Liu, Y.; Meng, X. Understanding effects of conductive additives in lithium-sulfur batteries. *Mater. Today Commun.* **2020**, *26*, 101934.

(9) Cao, J.; Chen, C.; Zhao, Q.; Zhang, N.; Lu, Q.; Wang, X.; Niu, Z.; Chen, J. A flexible nanostructured paper of a reduced graphene oxide−sulfur composite for high-performance lithium−sulfur batteries with unconventional configurations. *Adv. Mater.* **2016**, *28*, 9629−9636.

(10) Sun, L.; Wang, D.; Luo, Y.; Wang, K.; Kong, W.; Wu, Y.; Zhang, L.; Jiang, K.; Li, Q.; Zhang, Y.; Wang, J.; Fan, S. Sulfur Embedded in Mesoporous Carbon Nanotube Network as a Binder-Free Electrode for High Performance Lithium Sulfur Batteries. *ACS Nano* **2016**, *10*, 1300−1308.

(11) Tang, Z.; Liu, S.; Lu, Z.; Lin, X.; Zheng, B.; Liu, R.; Wu, D.; Fu, R. A simple self-assembly strategy for ultrahigh surface area nitrogen-doped porous carbon nanospheres with enhanced adsorption and energy storage performances. *Chem. Commun.* **2017**, *53*, 6764−6767.

(12) Li, S.; Fan, Z. Encapsulation methods of sulfur particles for lithium-sulfur batteries: A review. *Energy Storage Mater.* **2021**, *34*, 107−127.

(13) Sun, L.; Li, M.; Jiang, Y.; Kong, W.; Jiang, K.; Wang, J.; Fan, S. Sulfur nanocrystals confined in carbon nanotube network as a binder-free electrode for high-performance lithium sulfur batteries. *Nano Lett.* **2014**, *14*, 4044−4049.

(14) Scholz, J.; Kayaalp, B.; Juhl, A. C.; Clemens, D.; Fröba, M.; Mascotto, S. Severe loss of confined sulfur in nanoporous carbon for Li−S batteries under wetting conditions. *ACS Energy Lett.* **2018**, *3*, 387−392.

(15) Kresse, G.; Hafner, J. Ab initio molecular dynamics for liquid metals. *Phys. Rev. B: Condens. Matter Mater. Phys.* **1993**, *47*, 558−561.

(16) Kresse, G.; Hafner, J. Ab Iinitio molecular-dynamics simulation of the liquid-metal−amorphous-semiconductor transition in germanium. *Phys. Rev. B: Condens. Matter Mater. Phys.* **1994**, *49*, 14251−14269.

(17) Kresse, G.; Furthmüller, J. Efficient iterative schemes for ab initio total-energy calculations using a plane-wave basis set. *Phys. Rev. B: Condens. Matter Mater. Phys.* **1996**, *54*, 11169−11186.

(18) Kresse, G.; Furthmüller, J. Efficiency of ab-initio total energy calculations for metals and semiconductors using a plane-wave basis Set. *Comput. Mater. Sci.* **1996**, *6*, 15−50.

(19) Perdew, J. P.; Burke, K.; Ernzerhof, M. Generalized gradient approximation made simple. *Phys. Rev. Lett.* **1996**, *77*, 3865−3868.

(20) Kresse, G.; Joubert, D. From ultrasoft pseudopotentials to the projector augmented-wave method. *Phys. Rev. B: Condens. Matter Mater. Phys.* **1999**, *59*, 1758−1775.

(21) Grimme, S.; Antony, J.; Ehrlich, S.; Krieg, H. A consistent and accurate ab initio parametrization of density functional dispersion correction (DFT-D) for the 94 elements H-Pu. *J. Chem. Phys.* **2010**, *132*, 154104.

(22) Becke, A. D.; Johnson, E. R. Exchange-hole dipole moment and the dispersion interaction. *J. Chem. Phys.* **2005**, *122*, 154104.

(23) Monkhorst, H. J.; Pack, J. D. Special points for Brillouin-zone integrations. *Phys. Rev. B: Condens. Matter Mater. Phys.* **1976**, *13*, 5188−5192.

(24) Błonski, P.; Łodziana, Z. First-principles study of LiBH4 nanoclusters interaction with models of porous carbon and silica scaffolds. *Int. J. Hydrogen Energy* **2014**, *39*, 9848−9853.

(25) Guo, Q.; Li, S.; Liu, X.; Lu, H.; Chang, X.; Zhang, H.; Zhu, X.; Xia, Q.; Yan, C.; Xia, H. Ultrastable sodium−sulfur batteries without polysulfides formation using slit ultramicropore carbon carrier. *Adv. Sci.* **2020**, *7*, 1903246.

(26) Yang, C.-P.; Yin, Y.-X.; Guo, Y.-G.; Wan, L.-J. Electrochemical (de)lithiation of 1D sulfur chains in Li-S batteries: a model system study. *J. Am. Chem. Soc.* **2015**, *137*, 2215−2218.

(27) Qu, Y.; Zhang, Z.; Zhang, X.; Ren, G.; Wang, X.; Lai, Y.; Liu, Y.; Li, J. Synthesis of hierarchical porous honeycomb carbon for lithium-sulfur battery cathode with high rate capability and long cycling stability. *Electrochim. Acta* **2014**, *137*, 439−446.

(28) K, B.; R, S.; N, K. Exploration of microporous bio-carbon scaffold for efficient utilization of sulfur in lithium-sulfur system. *Electrochim. Acta* **2016**, *209*, 171−182.

(29) Seo, D. H.; Rider, A.; Zhao, J.; Kumar, S.; Ostrikov, K. Plasma break-down and re-build: same functional vertical graphenes from diverse natural precursors. *Adv. Mater.* **2013**, *25*, 5638−5642.

(30) Wang, Y.-X.; Huang, L.; Sun, L.-C.; Xie, S.-Y.; Xu, G.-L.; Chen, S.-R.; Xu, Y.-F.; Li, J.-T.; Chou, S.-L.; Dou, S.-X.; Sun, S.-G. Facile synthesis of a interleaved expanded graphite- embedded sulphur nanocomposite as cathode of Li−S batteries with excellent lithium storage performance. *J. Mater. Chem.* **2012**, *22*, 4744−4750.

(31) Okpalugo, T. I. T.; Papakonstantinou, P.; Murphy, H.; McLaughlin, J.; Brown, N. M. D. High resolution XPS character- ization of chemical functionalized MWCNTs and SWCNTs. *Carbon* **2005**, *43*, 153−161.

(32) Elazari, R.; Salitra, G.; Garsuch, A.; Panchenko, A.; Aurbach, D. Sulfur-impregnated activated carbon fiber cloth as a binder-free cathode for rechargeable Li-S batteries. *Adv. Mater.* **2011**, *23*, 5641−5644.

(33) Wang, X.; Zhang, Y.; Chang, Q.; Wu, Y.; Lei, W.; Zou, Y.; Ma, Z.; Pan, Y. Porous biochar nanosheets loaded with Fe3C particles accelerate electrochemical reactions and their applications in Li−S batteries. *Sustain. Energy Fuels* **2021**, *5*, 4346−4354.

(34) Xu, R.; Zhang, K.; Wei, R.; Yuan, M.; Zhang, Y.; Liang, F.; Yao, Y. High-capacity flour-based nano-Si/C composite anode materials for lithium-ion batteries. *Ionics* **2020**, *26*, 1−11.

(35) Irvine, J. T. S.; Sinclair, D. C.; West, A. R. Electroceramics: characterization by impedance spectroscopy. *Adv. Mater.* **1990**, *2*, 132−138.

(36) Zhu, J.; Lu, L.; Zeng, K. Nanoscale mapping of lithium-ion diffusion in a cathode within an all-solid-state lithium-ion battery by advances scanning probe microscopy techniques. *ACS Nano* **2013**, *7*, 1666−1675.

(37) Yan, Y.; Wei, Y.; Li, Q.; Shi, M.; Zhao, C.; Chen, L.; Fan, C.; Yang, R.; Xu, Y. Activated porous carbon materials with ultrahigh specific surface area derived from banana peels for high-performance lithium−sulfur batteries. *J. Mater. Sci. Mater. Electron.* **2018**, *29*, 11325−11335.